Supporting Information for

High oxide ion conductivity in the layer-structured $Bi_4Ti_3O_{12}$-based ferroelectric ceramics

Changbai Long, ∗[a, b] **Wei Ren,** [b] **Yiwen Li,** [c] **Laijun Liu,** [d] **Yuanhua Xia,** [e] **Huiqing Fan** ∗[f]

[a] *School of Advanced Materials and Nanotechnology, Xidian University, Xi'an, 710071, China*
[b] *Electronic Material Research Laboratory, Key Laboratory of the Ministry of Education & International Center for Dielectric Research, Xi'an Jiaotong University, Xi'an 710049, China*
[c] *Science and Technology on plasma dynamics laboratory, Air Force Engineering University, Xi'an, 710038, China*
[d] *Key laboratory of Nonferrous Materials and New Processing Technology, Ministry of Education, College of Materials Science and Engineering, Guilin University of Technology, Guilin 541004, China*
[e] *Institute of Nuclear Physics and Chemistry, China Academy of Engineering Physics (CAPE), Mianyang, Sichuan 621900, China*
[f] *State Key Laboratory of Solidification Processing, School of Materials Science and Engineering, Northwestern Polytechnical University, Xi'an 710072, PR China*

Corresponding Author:

∗Long, C. B., *E-mail*: longchangbai@126.com; Fan. H. Q., *E-mail*: hqfan3@163.com.

Characterization and measurements

Powder X-ray diffraction (XRD) data were collected by using an automated diffractometer (X'Pert PRO MPD, Philips, Eindhoven, The Netherlands) with a nickel filter (Cu Kα radiation) at room temperature. For checking phase purity and calculating lattice parameters, data of the prepared oxides were collected in 2θ range of 10-110 ° with a step size of about 0.02 °, the entire run lasting about 2 h. For structural refinement, data of $B_{0.97}T_{0.72}Mg_{0.03}$ were collected in 2θ range of 10-130 ° with a step size of 0.02 ° and a step time of 10 s at room temperature. Raman spectra were obtained with an instrument (LabRAM HR800, Horiba Jobin Yvon, Lyon, France) in a backward scattering geometry (the exciting source was the 514.5 nm line from an argon ion laser). Cross-section scanning electron microscope (SEM) images were performed by using a scanning electron microscope (SEM; JSM-5610, JEOL, Tokyo, Japan) instrument equipped with energy-dispersive x-ray spectroscopy (EDS). EPR spectra were recorded using a high-sensitivity X-band (about 9.3 GHz) electron paramagnetic resonance system (JES-FA200, JEOL, Japan) at 100 K. Ferroelectric properties were measured by using a ferroelectric analyzer (TF-2000, Aix ACCT, Aachen, Germany).

Phase purity and structure

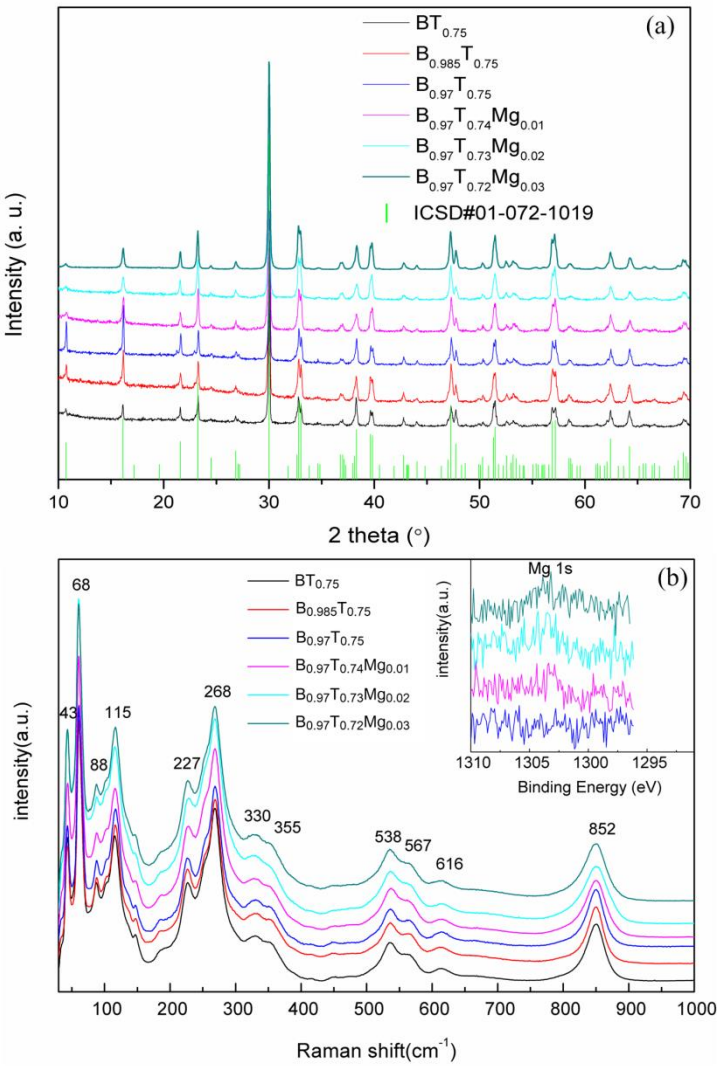

Fig. S1 (a) Powder XRD patterns and (b) Raman spectra of $B_{1-x}T_{0.75-y}Mg_y$ of $B_{1-x}T_{0.75-y}Mg_y$. In (a), an inset shows XPS spectra associated with the Mg 1*s* core level photoemission.

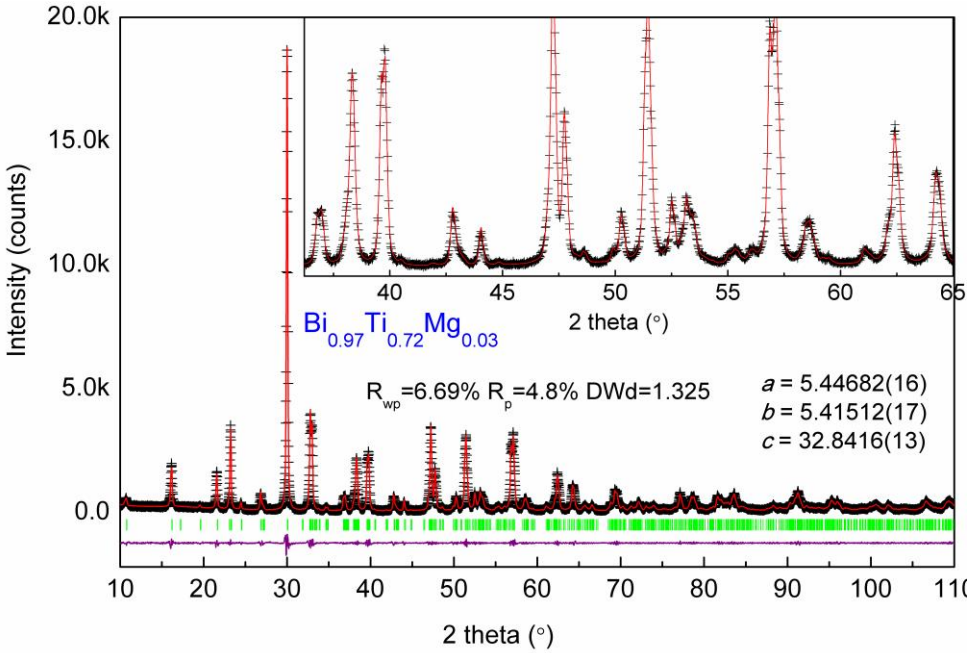

Fig. S2 Neutron diffraction refinements for $B_{0.97}T_{0.72}Mg_{0.03}$, with insets showing regionally enlarged drawing.

Fig. S1a shows powder XRD patterns of $B_{1-x}T_{0.75-y}Mg_y$ (x = 0-0.03, y = 0-0.03). For each composition, all diffraction peaks can be referred to the $Bi_4Ti_3O_{12}$ orthorhombic structure (ICSD#01-072-1019), and no any evidence for impurity phases is seen. Raman spectra of all compositions exhibit similar phonon modes associated with the orthorhombic structure, [1-3] and no any additional phonon mode is observed, as shown in Fig. S1b. As indicated by XPS results, there is a small peak associated with the Mg 1*s* core level photoemission observed for Mg-doped compositions (inset of Fig. S1a). This is indicative of incorporation of Mg in the structure of $BT_{0.75}$. Also, it is not indicative of any impurity phase in the high-intensity XRD pattern of $B_{0.97}T_{0.72}Mg_{0.03}$, and refining XRD profile with a Le-Bail fit (GSAS-EXPGUI program) [4,5] for $B_{0.97}T_{0.72}Mg_{0.03}$ results in that the calculated data well fit for the experimental data, as shown in Fig. S2. These results show no evidence for any impurity phases caused by Bi deficiency and Mg doping.

However, SEM images and EDS line scans revealed some amounts of Ti-rich-and-Bi-deficient secondary phases (dark) in Bi-deficient compositions (Fig. S3). Point EDS analyses show that both $Bi_2Ti_2O_7$ and $Bi_2Ti_4O_{11}$ exist in $B_{0.97}T_{0.75}$, but $Bi_2Ti_2O_7$ primarily exist in $B_{0.985}T_{0.75}$. Further Mg doping in $B_{0.97}T_{0.75-y}Mg_y$ results in the generation of $MgTiO_3$ ($y \geq 0.02$). Furthermore, compositional analysis by EDS reveal that real composition in $BT_{0.75}$, $B_{0.985}T_{0.75}$ and $B_{0.97}T_{0.75}$ is almost identical and normalized Bi/Ti ratio of the main phase is ~1.304-1.31. For $B_{0.97}T_{0.74}Mg_{0.01}$ and

$B_{0.97}T_{0.73}Mg_{0.02}$, compositional analysis shows that normalized average Mg/Ti ratio is close to that in the corresponding nominal composition. But this value is lower than the theoretical ratio for $B_{0.97}T_{0.72}Mg_{0.03}$.

By further thermal etching, cross-section SEM images of four selected compositions are shown in Fig. S4. It is observed that pure and Bi-deficient BiT compositions show comparable grains with sizes of ~10-40 μm (Fig. S4a and S4b). In contrast, grain growth of the ceramics is suppressed by Mg doping, and the grain sizes of $B_{0.97}T_{0.73}Mg_{0.02}$ and $B_{0.97}T_{0.72}Mg_{0.03}$ are ~5-20 μm (Fig. S4c and S4d).

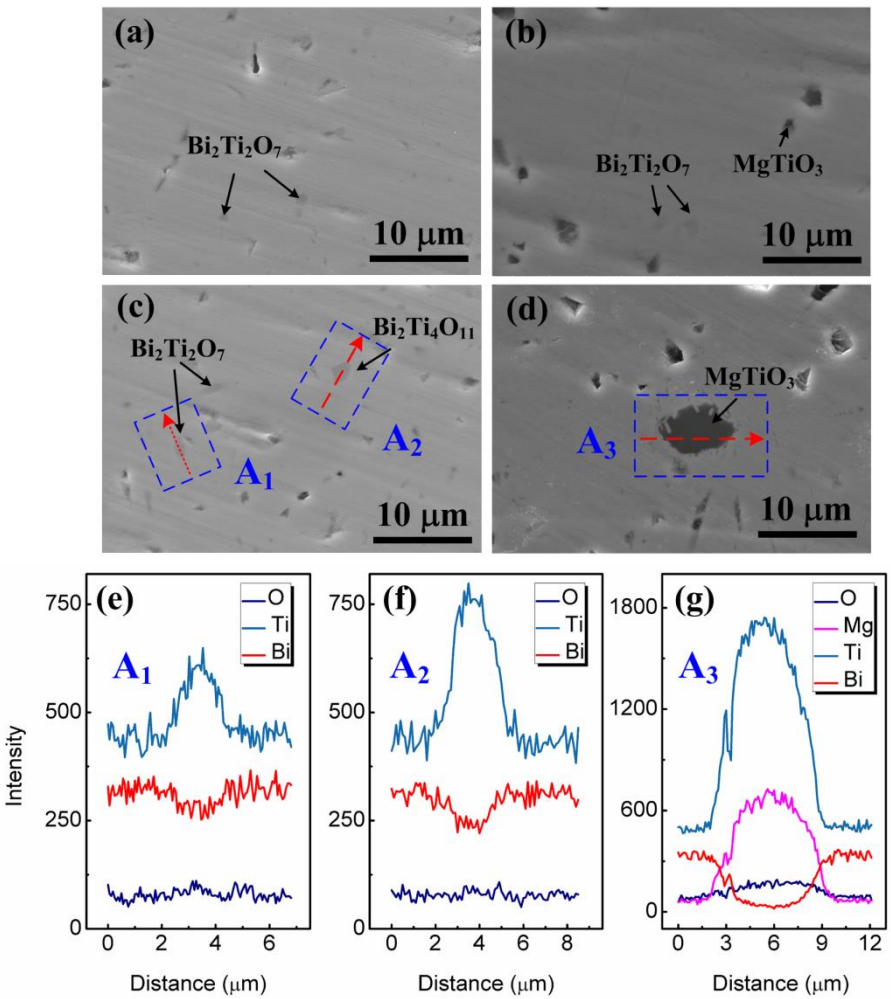

Fig. S3 Cross-section SEM images (secondary electron) of (a) $B_{0.985}T_{0.75}$, (b) $B_{0.97}T_{0.75}$, (c) $B_{0.97}T_{0.73}Mg_{0.02}$ and (d) $B_{0.97}T_{0.72}Mg_{0.03}$ (polished without thermal etching). EDS line scans of regions (e) A_1, (f) A_2 and (g) A_3.

Table S1 Cation composition analyses in $B_{1-x}T_{0.75-y}Mg_y$ (x = 0-0.03, y = 0-0.03). EDS data for grain composition were obtained by measurements on 10 randomly selected areas within grains. The mean value and standard deviation are listed. The theoretical density was determined by using the obtained lattice parameters and the experimental density was measured by the Archimedes method.

Compositions	Bi (*at*. %)	Ti (*at*. %)	Mg (*at*. %)	Real compositions	Relative density (%)
$BT_{0.75}$	56.69 (±0.38)	43.31 (±0.39)	––	$Bi_{0.982}Ti_{0.75}O_{2.973}$	95.8
$B_{0.985}T_{0.75}$	56.62 (±0.37)	43.38 (±0.48)	––	$Bi_{0.979}Ti_{0.75}O_{2.969}$	96.6
$B_{0.97}T_{0.75}$	56.59 (±0.31)	43.41 (±0.43)	––	$Bi_{0.978}Ti_{0.75}O_{2.967}$	95.7
$B_{0.97}T_{0.74}Mg_{0.01}$	56.56 (±0.29)	42.82 (±0.51)	0.62 (±0.34)	$Bi_{0.976}Ti_{0.739}Mg_{0.011}O_{2.951}$	97.1
$B_{0.97}T_{0.73}Mg_{0.02}$	56.51 (±0.24)	42. 45 (±0.38)	1.04 (±0.31)	$Bi_{0.975}Ti_{0.732}Mg_{0.018}O_{2.936}$	96.4
$B_{0.97}T_{0.72}Mg_{0.03}$	56.59 (±0.33)	42.45 (±0.54)	0.96 (±0.28)	$Bi_{0.979}Ti_{0.733}Mg_{0.017}O_{2.949}$	93.9

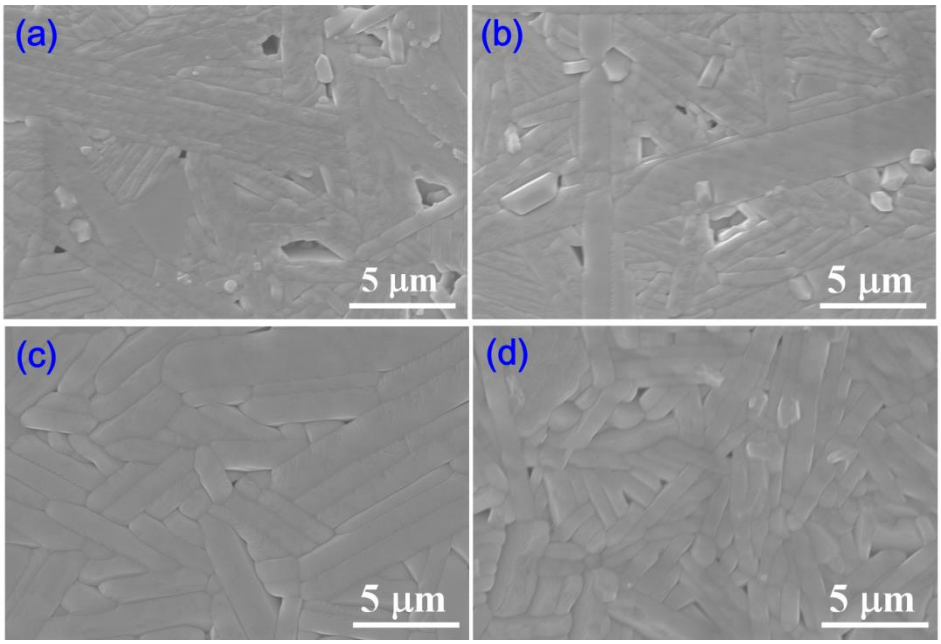

Fig. S4 Cross-section SEM images of (a) $BT_{0.75}$, (b) $B_{0.97}T_{0.75}$, (c) $B_{0.97}T_{0.73}Mg_{0.02}$ and (d) $B_{0.97}T_{0.72}Mg_{0.03}$. All samples were polished and thermally etched prior to SEM measurements.

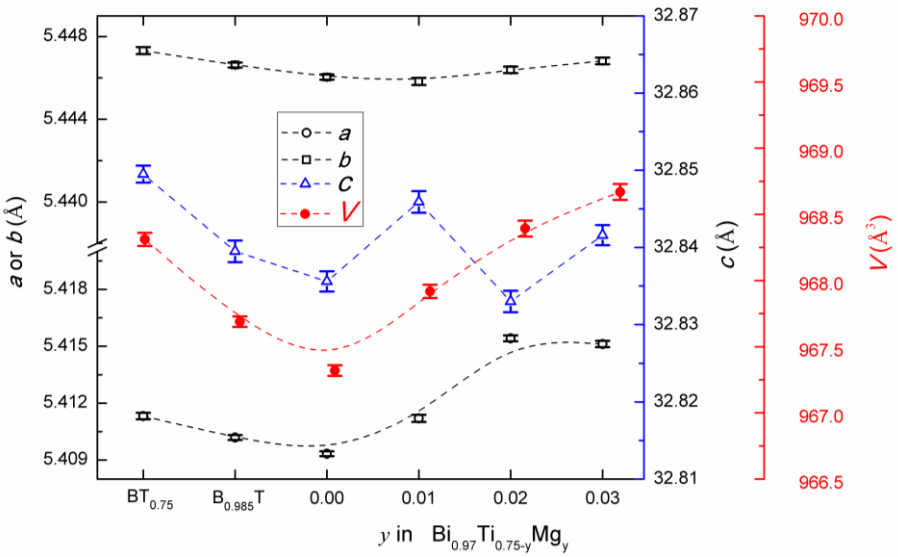

Fig. S5 Evolutions in lattice parameters (*a*, *b*, *c*) and unit cell volume (*V*) with variable *x* and *y* in $B_{1-x}T_{0.75-y}Mg_y$.

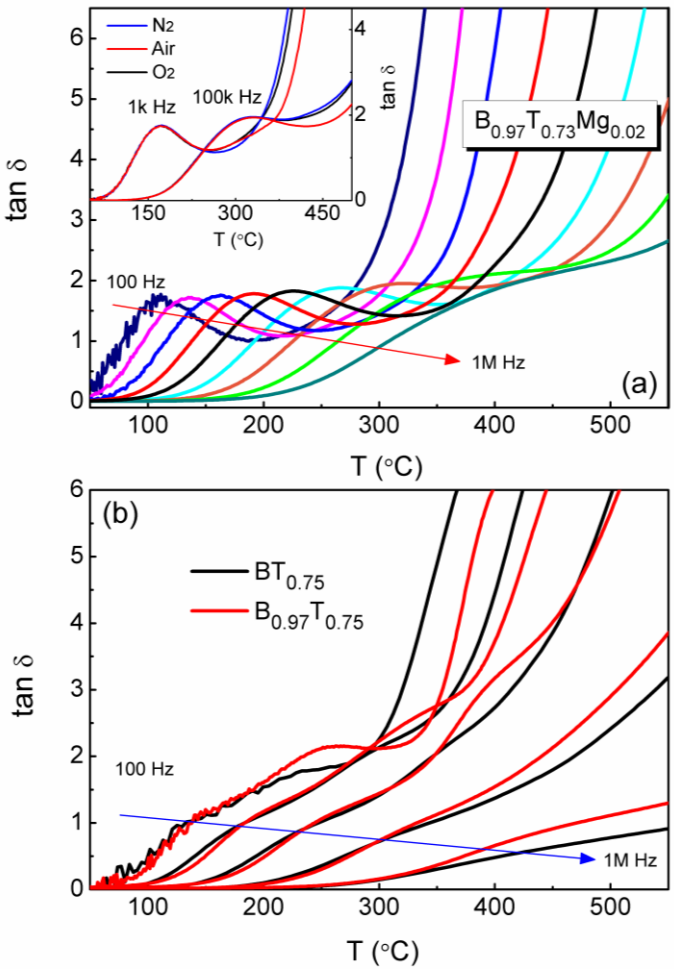

Fig. S6 Frequency-dependent loss peaks for (a) $B_{0.97}T_{0.73}Mg_{0.02}$ and (b) $BT_{0.75}$ and $B_{0.97}T_{0.75}$ in the low temperature segment. In (a), an inset shows low-temperature loss peak for the air-, O_2- and N_2-processed $B_{0.97}T_{0.73}Mg_{0.02}$ at 1k and 100k Hz, which was annealed at 850 °C for 4h in respective atmosphere prior to the measurements.

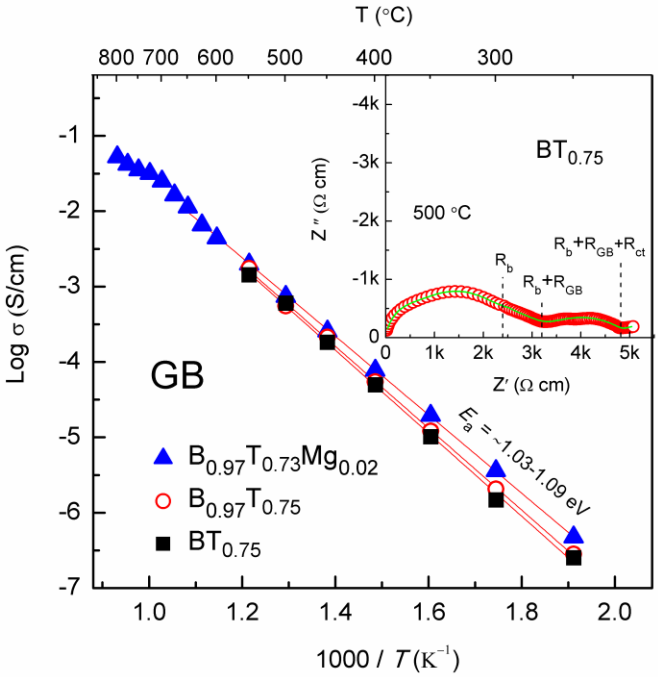

Fig. S7 Arrhenius plots of grain boundary conductivity (σ_{gb}) for $BT_{0.75}$, $B_{097}T_{0.75}$, $B_{0.97}T_{0.73}Mg_{0.02}$, and an inset shows complex *Z** plot of $BT_{0.75}$ at 500 °C.

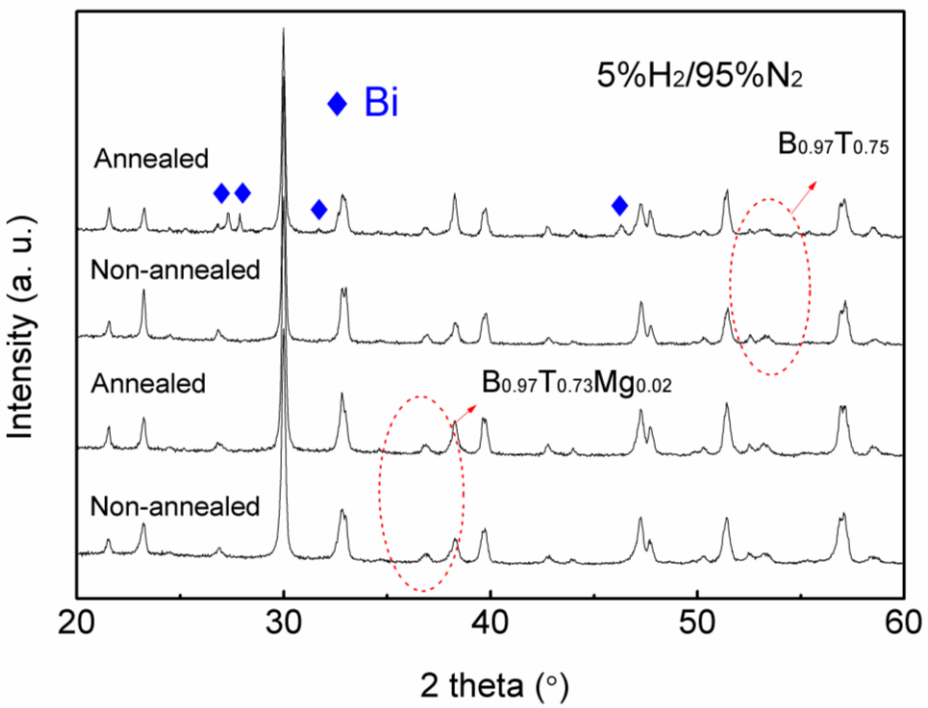

Fig. S8 XRD patterns of $B_{0.97}T_{0.75}$ and $B_{0.97}T_{0.73}Mg_{0.02}$ before and after annealing in a $5\%H_2/95\%N_2$ reducing atmosphere at 650 ℃ for 6 h.

Neutron diffraction refinements

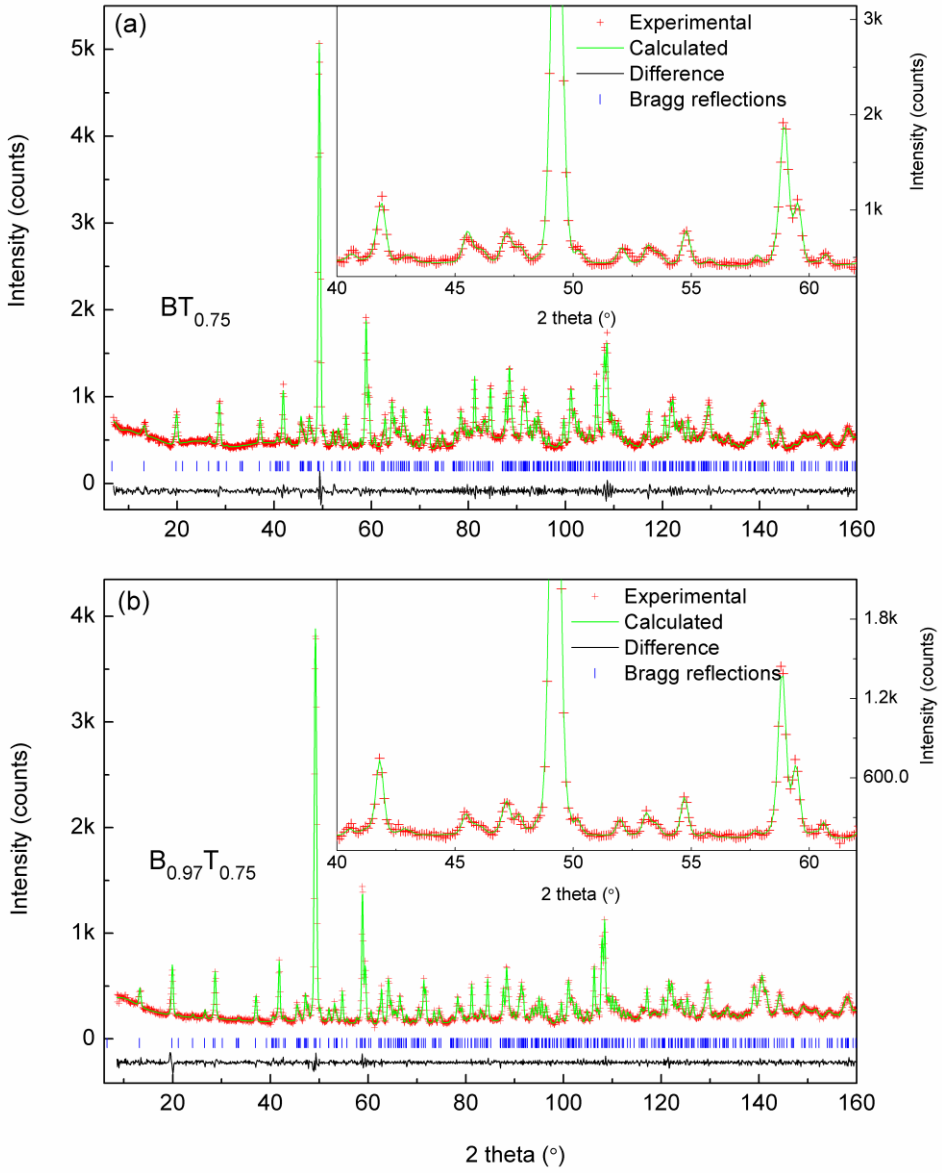

Fig. S9 Neutron diffraction refinements for (a) $BT_{0.75}$ and (b) $B_{0.97}T_{0.75}$ at room temperature (25 ℃).

Table S2 Details of Neutron diffraction refinements for $BT_{0.75}$, $B_{0.97}T_{0.75}$ and $B_{0.97}T_{0.73}Mg_{0.02}$

composition	$BT_{0.75}$	$B_{0.97}T_{0.75}$	$B_{0.97}T_{0.73}Mg_{0.02}$		
Crystal system	orthorhombic	orthorhombic	orthorhombic	orthorhombic	tetragonal
Space group	*B2cb*	*B2cb*	*B2cb*	*B2cb*	*I4/mmm*
Temperature (K)	298	298	298	773	1073
a (Å)	5.4473(2)	5.4464(2)	5.4463(2)	5.4572(2)	3.86540(8)
b (Å)	5.4110(2)	5.4100(1)	5.4160(2)	5.4388(2)	––
c (Å)	32.850(1)	32.8387(9)	32.830(2)	33.005(2)	33.260(2)
V (Å^3)	968.26(5)	967.60(4)	968.39(8)	979.60(9)	496.94(4)
R_{wp} (%)	3.81	4.96	4.31	4.41	4.64
R_p (%)	2.96	3.71	3.30	3.42	3.52
D_{wd}	1.207	1.431	1.636	1.289	1.068
No. of formula units per unit cell, *Z*	4	4	4	4	4
No. of data	1728	1891	1739	1811	1778

Table S3 Atomic coordinates, atomic occupancies and isotropic thermal parameters of $B_{0.97}T_{0.73}Mg_{0.02}$ at room temperature (25 ℃)

Atom	Site	*x*	*y*	*z*	U_{iso} (Å^2)	Occupancy
Bi1	8	0	0.994(1)	0.0680(2)	0.0077(9)	0.982(8)
Bi2	8	0.996(2)	0.019 (2)	0.2106(2)	0.022 (2)	0.961(9)
Ti1	4	0.051(2)	0	0.5	0.012(5)	1
Ti2/Mg2	8	0.049(3)	1.006(4)	0.3720(4)	0.001(1)	0.96/0.04
O1	8	0.319 (3)	0.254(3)	0.0081(4)	0.039 (3)	1
O2	8	0.267(3)	0.245(3)	0.2495(5)	0.013(2)	0.942(9)
O3	8	0.078(2)	1.069(2)	0.4406(4)	0.022(2)	0.973(8)
O4	8	1.049 (2)	0.953(2)	0.3205(3)	0.013 (2)	1
O5	8	0.285(2)	0.233(2)	0.1147(3)	0.007(2)	0.985(9)
O6	8	0.350(2)	0.2972(19)	0.8756(4)	0.005(2)	0.975(9)

Table S4 Atomic coordinates, atomic occupancies and isotropic thermal parameters of $B_{0.97}T_{0.73}Mg_{0.02}$ at 500 ℃

Atom	Site	*x*	*y*	*z*	U_{iso} (Å^2)	Occupancy
Bi1	8	0	0.986(2)	0.0685(3)	0.038(1)	0.978(8)
Bi2	8	1.000(2)	0.022(2)	0.2097(2)	0.038(1)	0.965(8)
Ti1	4	0.0482(2)	0	0.5	0.059(4)	1
Ti2/Mg2	8	0.032(2)	1.010(4)	0.3728(4)	0.003(2)	0.96/0.04
O1	8	0.299(3)	0.245(5)	0.0074(6)	0.096(3)	1
O2	8	0.255(2)	0.246(4)	0.2475(4)	0.014(2)	0.948(9)
O3	8	0.063(2)	1.044(2)	0.4432(4)	0.036(2)	0.967(9)
O4	8	1.036(2)	0.937(2)	0.3219(3)	0.020(2)	1
O5	8	0.278(2)	0.242(4)	0.1133(3)	0.017(2)	0.973(9)
O6	8	0.334(2)	0.292(3)	0.8737(5)	0.049(2)	0.987(9)

Table S5 Atomic coordinates, atomic occupancies and anisotropic thermal parameters of $B_{0.97}T_{0.73}Mg_{0.02}$ at 800 ℃.

Atom	Site	*x*	*y*	*z*	U_{11} (Å^2)	U_{22} (Å^2)	U_{33}(Å^2)	Occupancy
Bi1	4	0.5	0.5	0.0670(4)	0.107(3)	0.107(3)	0.089(5)	0.978(9)
Bi2	4	0.5	0.5	0.2093(2)	0.134(5)	0.134(5)	0.021(5)	0.962(9)
Ti1	2	0.5	0.5	0.5	0.012(4)	0.012(4)	0.092(6)	1
Ti2/Mg2	4	0.5	0.5	0.3734(5)	0.003(3)	0.003(3)	0.063(6)	0.96/0.04
O1	4	0.5	0	0	0.018(5)	0.268(5)	0.032(7)	0.979(3)
O2	4	0.5	0	0.25	0.049(3)	0.049(3)	0.039(6)	0.943(9)
O3	4	0.5	0.5	0.4397(5)	0.073(4)	0.073(4)	0.100(4)	0.985(3)
O4	4	0.5	0.5	0.3213(5)	0.103(5)	0.103(5)	0.109(9)	0.990(3)
O5	8	0.5	0	0.1168(3)	0.179(6)	0.046(4)	0.081(7)	0.984(3)

Table S6 Atomic coordinates, atomic occupancies and isotropic thermal parameters of $BT_{0.75}$ at room temperature

Atom	Site	*x*	*y*	*z*	$100U_{iso}$ (Å^2)	Occupancy
Bi1	8	0	0.998(1)	0.0669(1)	0.0093(8)	0.986(6)
Bi2	8	0.999(1)	0.012(1)	0.2110(1)	0.0136(9)	0.977(5)
Ti1	4	0.055(3)	0	0.5	0.014(4)	1
Ti2	8	0.053(2)	0.998(3)	0.3706(3)	0.007(3)	1
O1	8	0.322(2)	0.247(2)	0.0071(2)	0.014(2)	1
O2	8	0.274(2)	0.250(2)	0.2502(3)	0.007 (1)	0.969(8)
O3	8	0.085(1)	1.058(1)	0.4416(2)	0.008(1)	0.979(8)
O4	8	1.060(2	0.950(1)	0.3188(2)	0.005(1)	1
O5	8	0.292(2)	0.231(2)	0.1121(2)	0.005(2)	1
O6	8	0.367(2)	0.303(2)	0.8762(3)	0.007(2)	1

Table S7 Atomic coordinates, atomic occupancies and isotropic thermal parameters of $B_{0.97}T_{0.75}$ at room temperature

Atom	Site	*x*	*y*	*z*	U_{iso} (Å^2)	Occupancy
Bi1	8	0	0.999(1)	0.0668(1)	0.0051(6)	0.979(6)
Bi2	8	1.001(1)	0.020(1)	0.2115(1)	0.0089(6)	0.966(5)
Ti1	4	0.040(2)	0	0.5	0.006(2)	1
Ti2	8	0.053(2)	1.003(2)	0.3717(2)	0.002(2)	1
O1	8	0.325(2)	0.258(1)	0.0079(2)	0.019(2)	1
O2	8	0.272(1)	0.245(1)	0.2508(3)	0.003(1)	0.949(8)
O3	8	0.091(1)	1.059(1)	0.4414(2)	0.010(1)	0.968(9)
O4	8	1.057(1)	0.948(1)	0.3187(2)	0.010(1)	1
O5	8	0.295(1)	0.224(1)	0.1118(2)	0.011(1)	1
O6	8	0.357(1)	0.296(1)	0.8771(2)	0.002(1)	1

Table S8 Selected bond lengths (Å) and angles (°) for $BT_{0.75}$, $B_{0.97}T_{0.75}$ and $B_{0.97}T_{0.73}Mg_{0.02}$.

Bond	$BT_{0.75}$	$B_{0.97}T_{0.75}$	$B_{0.97}T_{0.73}Mg_{0.02}$		
	(25 °C)	(25 °C)	25 °C	500 °C	800 °C
Bi1-O1	2.956(9)	2.974(8)	2.98(1)	2.951(7)	2.949(9)×4
Bi1-O1	3.275(9)	3.330(8)	3.33(1)	3.243(8)	
Bi1-O1	2.59(1)	2.527(8)	2.59(1)	2.721(8)	
Bi1-O1	2.95(1)	2.938(8)	2.98(1)	3.033(8)	
Bi1-O3	2.44(1)	2.447(9)	2.36(1)	2.457(9)	2.742(2)×4
Bi1-O3	3.08(1)	3.081(9)	3.16(1)	3.080(9)	
Bi1-O3	2.297(8)	2.267(7)	2.33(1)	2.420(7)	
Bi1-O3	3.214(8)	3.245(7)	3.19(1)	3.102(6)	
Bi1-O5	2.51(1)	2.496(8)	2.54(1)	2.532(7)	2.55(1)×4
Bi1-O5	2.38(1)	2.381(8)	2.43(1)	2.417(8)	
Bi1-O6	3.18 (1)	3.118(8)	3.09(1)	3.041(7)	
Bi1-O6	2.27(1)	2.283(8)	2.29(1)	2.361(8)	
Bi2-O2	2.35(1)	2.305(9)	2.30(2)	2.232(7)	2.359(5)×4
Bi2-O2	2.43(1)	2.432(9)	2.47(2)	2.489(8)	
Bi2-O2	2.27(1)	2.271(9)	2.30(2)	2.430(8)	
Bi2-O2	2.20 (1)	2.203(9)	2.19(2)	2.219(7)	
Bi2-O4	3.21(1)	3.262(8)	3.24(1)	3.35(1)	2.917(6)×4
Bi2-O4	2.58(1)	2.538(8)	2.58(1)	2.47(1)	
Bi2-O4	2.59(1)	2.623(9)	2.64(1)	2.746(9)	
Bi2-O4	3.21(1)	3.187(9)	3.18(1)	3.115(8)	
Bi2-O6	3.16(1)	3.246(8)	3.17(1)	3.157(7)	
Ti1-O1×2	2.01(2)	2.049(13)	2.00(1)	1.96(2)	1.93270(4)
Ti1-O1×2	1.86(2)	1.838(12)	1.89(1)	1.92(1)	1.93270(4)
Ti1-O3×2	1.950(8)	1.969(7)	1.99(1)	1.89(1)	1.978(1)
Ti2-O3	2.36(1)	2.319(10)	2.28(1)	2.34(1)	2.21(2)
Ti2-O4	1.72(1)	1.764(9)	1.716(9)	1.73(1)	1.73(2)
Ti2-O5	2.03(2)	2.07(1)	2.01(1)	2.03(2)	1.960(3)×4
Ti2-O5	1.97(2)	1.95(1)	1.98(1)	2.01(2)	
Ti2-O6	2.03(2)	1.99(1)	1.96(1)	1.97(2)	
Ti2-O6	1.94(2)	1.93(1)	1.92(1)	1.88(2)	
Ti1-O1-Ti1	165.8(5)	161.7(5)	163.3(8)	165.5(9)	180.0
Ti1-O3-Ti2	160.6(6)	158.4(5)	158.8(5)	166.4(7)	180.0
Ti2-O5-Ti2	146.3(7)	148.0(5)	153.8(5)	153.6(6)	160.7(9)
Ti2-O6-Ti2	151.7(7)	154.9(5)	156.3(6)	158.3(9)	

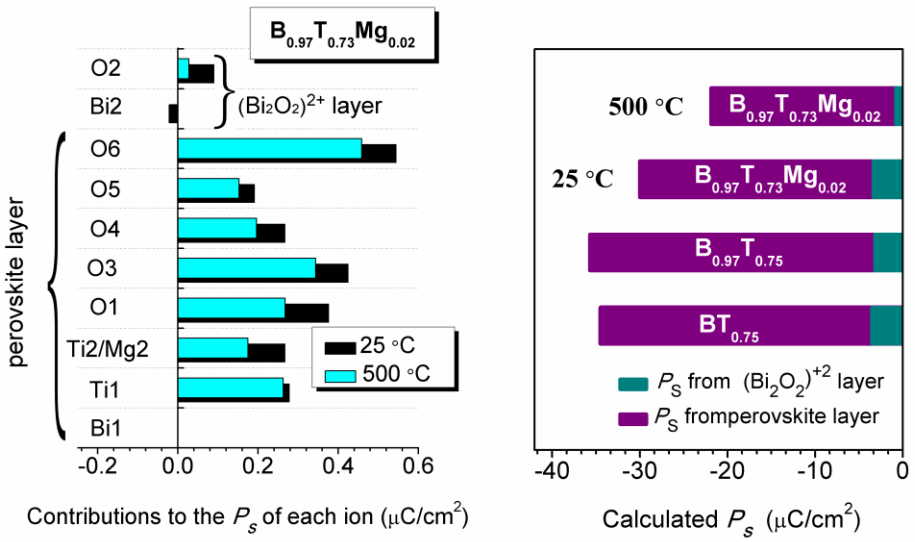

Fig. S10 (a) Ion displacement of each ion in $B_{0.97}T_{0.73}Mg_{0.02}$ at 25 ℃ and 500 ℃ in the *a*-axis direction (the position of the Bi1 site on the *a* axis is fixed at the origin.). (b) Calculated P_s of $BT_{0.75}$, $B_{0.97}T_{0.75}$ and $B_{0.97}T_{0.73}Mg_{0.02}$.

P_s along the a-axis direction for $BT_{0.75}$, $B_{0.97}T_{0.75}$ and $B_{0.97}T_{0.73}Mg_{0.02}$ was calculated on the basis of ion displacements from the parent-phase structure (Table S2-S7 in Supporting Information) by using Shimakawa's mode, [6]

$$P_s = \sum_i \frac{m_i \times \Delta x_i \times Q_i e}{V} \qquad (2)$$

where m_i is the site multiplicity, $\triangle x_i$ is the atomic displacement along the *a* axis from the corresponding position in the parent structure, $Q_i e$ is the ionic charge for the *i* th constituent ion, and *V* is the volume of the unit cell.

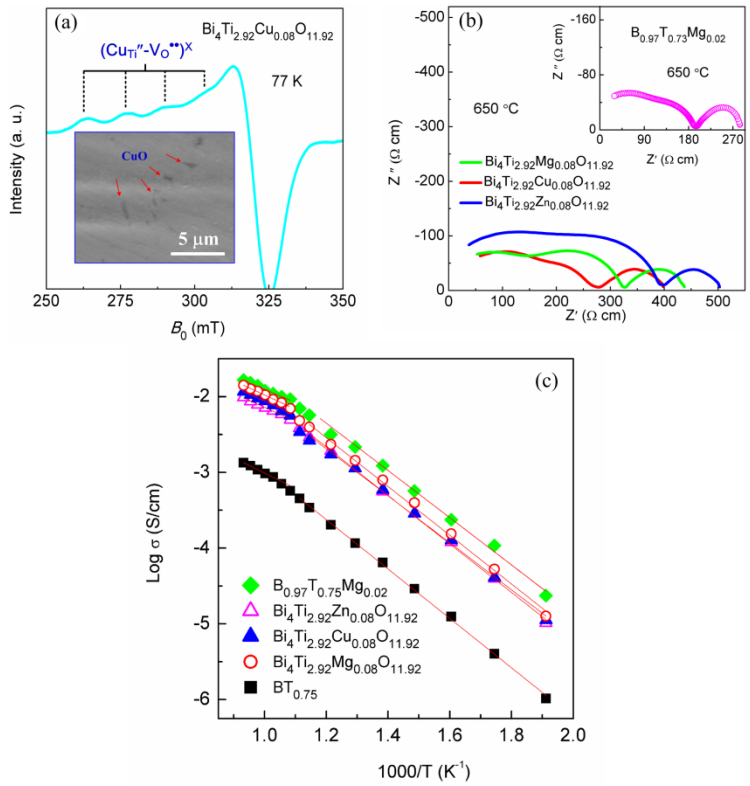

Fig. S11 (b) *X*-band (9.18 GHz) EPR spectra of $Bi_4Ti_{2.92}Cu_{0.08}O_{11.92}$ at 100 K with an inset showing cross-section SEM image of it (polished without thermal etching). (b) 650 ℃ complex *Z** plots of singly Mg-, Cu- and Zn-doped compositions as well as $B_{0.97}Ti_{0.73}Mg_{0.02}$ (inset). (c) Compared bulk conductivity Arrhenius plots for singly Mg-, Cu- and Zn-doped compositions as well as $BT_{0.75}$ and $B_{0.97}T_{0.73}Mg_{0.02}$.

In order to clarify the crucial effects of Mg doping on the electrical properties of $BT_{0.75}$, only B-site doped $BT_{0.75}$ with compositions of $Bi_4Ti_{2.92}M_{0.08}O_{11.92}$ (M= Mg, Cu and Zn) were prepared with the same ceramic processing route as $B_{0.97}T_{0.75-y}Mg_y$ (y = 0.01, 0.02 and 0.03). Inspection from EPR spectrum of $Bi_4Ti_{2.92}Cu_{0.08}O_{11.92}$ reveals that Cu^{2+} in replace of Ti^{4+} occupies at the B site and finally the formation of $(Cu_{Ti}''\text{-}V_O^{\bullet\bullet})^X$ defect dipole (Fig. S11a). And cross-section SEM image reveals that there are small amounts of impurity CuO in it (inset of Fig. S11a). Fig. S11b shows 650 ℃ complex Z* plots of $Bi_4Ti_{2.92}M_{0.08}O_{11.92}$ (M = Mg, Cu and Zn). It is clearly observed that Mg-, Cu- and Zn-doped compositions display similar impedance data with the same conduction mechanism as $B_{0.97}T_{0.73}Mg_{0.02}$ (inset of Fig. S11a). The size of high-frequency semicircle of them is approximate, which is associated with a bulk resistance of ~146-182 Ω cm. This value is higher than that of $B_{0.97}T_{0.73}Mg_{0.02}$ (~110 Ω cm) but much lower than that of $BT_{0.75}$ (~1760 Ω cm). Over the measured temperature range (250-800 ℃), extracted σ_b of $Bi_4Ti_{2.92}M_{0.08}O_{11.92}$ is slightly lower than that of $B_{0.97}T_{0.73}Mg_{0.02}$ (Fig. S11c). And associated E_a (0.36-0.38 eV and 0.62-0.65 eV above and below T_c, respectively) is consistent with that of $B_{0.97}T_{0.73}Mg_{0.02}$ (0.35 eV and 0.62 eV above and below T_c, respectively).

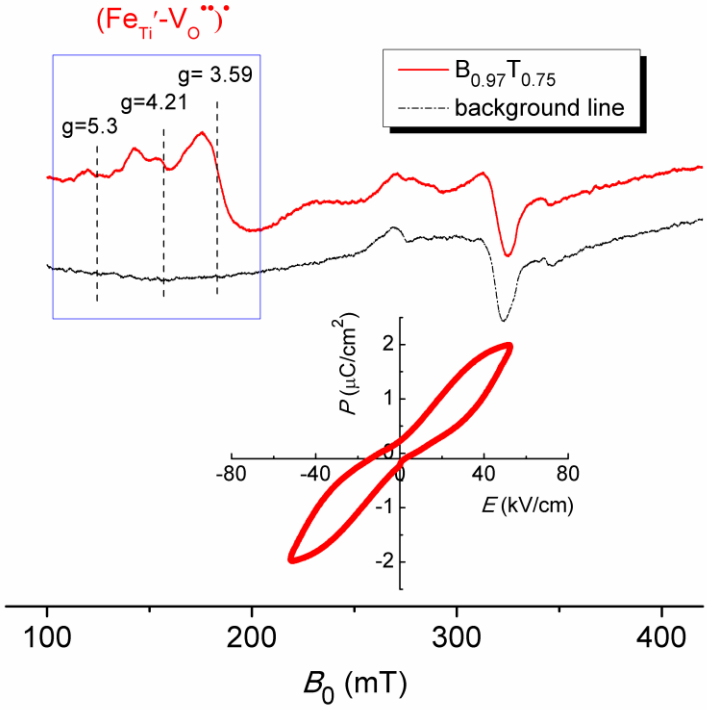

Fig. S12 *X*-band (9.18 GHz) EPR spectrum of $B_{0.97}T_{0.75}$ at 100 K with an inset showing its ferroelectric hysteresis (*P*-*E*) loop.

References:

1 H. Idink, V. Srikanth, B. William White, E. C. Subbarao, *J. Appl. Phys*., 1994, **76**, 1819.

2 K. Liang, Y. Qi, C. Lu, *J. Raman Spectrosc*., 2009, **40**, 2088–2091.

3 C. Y. Yau, R. Palan, K. Tran, and R. C. *Appl. Phys. Lett*., 2004, **85**, 4714-4716.

4 A. C. Larson, R. B. Von Dreele, *General Structure Analysis System (GSAS)*, 79-92 (Report No. LAUR-86-748) (Los Alamos National Laboratory), 2000.

5 B. H. Toby, *J. Appl. Cryst*., 2001, **34**, 210-213.

6 Y. Shimakawa, Y. Kubo, Y. Nakagawa, T. Kamiyama, H. Asano, F. Izumi, *Appl. Phys. Lett.*, 1999, **74**, 1904-1906.